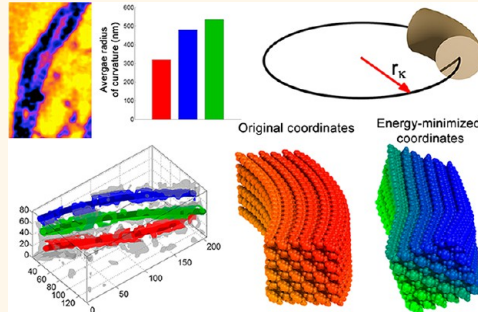


3D Electron Tomography of Pretreated Biomass Informs Atomic Modeling of Cellulose Microfibrils

Peter N. Ciesielski,^{†,*} James F. Matthews,[†] Melvin P. Tucker,[‡] Gregg T. Beckham,[‡] Michael F. Crowley,[†] Michael E. Himmel,[†] and Bryon S. Donohoe^{†,*}

[†]Biosciences Center, National Renewable Energy Laboratory, 15013 Denver West Parkway, Golden, Colorado 80401, United States, and [‡]National Bioenergy Center, National Renewable Energy Laboratory, 15013 Denver West Parkway, Golden, Colorado 80401, United States

ABSTRACT Fundamental insights into the macromolecular architecture of plant cell walls will elucidate new structure–property relationships and facilitate optimization of catalytic processes that produce fuels and chemicals from biomass. Here we introduce computational methodology to extract nanoscale geometry of cellulose microfibrils within thermochemically treated biomass directly from electron tomographic data sets. We quantitatively compare the cell wall nanostructure in corn stover following two leading pretreatment strategies: dilute acid with iron sulfate co-catalyst and ammonia fiber expansion (AFEX). Computational analysis of the tomographic data is used to extract mathematical descriptions for longitudinal axes of cellulose microfibrils from which we calculate their nanoscale curvature. These nanostructural measurements are used to inform the construction of atomistic models that exhibit features of cellulose within real, process-relevant biomass. By computational evaluation of these atomic models, we propose relationships between the crystal structure of cellulose I β and the nanoscale geometry of cellulose microfibrils.



KEYWORDS: transmission electron tomography · biomass nanostructure · cellulose microfibril · atomic modeling · biofuels · thermochemical pretreatment

The bulk properties of materials are dictated not only by their elemental composition and molecular connectivity, but also by their macromolecular architecture. A principal example of this is observed in plant cell walls, which are composite materials comprising biopolymers designed to serve multiple functions including structural support, microbial defense, and transport of water and nutrients throughout the organism. While the molecular composition¹ and microstructure² of several biomass varieties have been well-characterized, quantitative analysis of the higher-order nanoscale architecture of the cell wall remains elusive.³ However, many of the structural properties that impart recalcitrance to conversion into biofuels and chemicals exist at this length scale.⁴ Designing efficient and cost-effective catalysts and processes that specifically address the robust nanostructure of biomass is essential for the commercialization of biofuels from lignocellulosic biomass, which constitutes

an important step toward a diverse and economically viable renewable energy portfolio.⁵ Many current strategies for the catalytic deconstruction of the biopolymers composing lignocellulosic biomass employ thermochemical pretreatments⁶ to assist the penetration of enzymatic and chemical catalysts into the cell walls. Recent modeling studies have provided valuable insight for the optimization of biomass conversion processes,^{7–11} and this progress will be accelerated by accurate models of the macromolecular architecture of biomass developed by characterization and analysis techniques specialized for nanostructural investigations. Existing models of biomass nanostructure based on experimental observations^{12,13} are conceptually useful, but have limited utility for the inherently quantitative task of process optimization, and do not allow for the rigorous computational evaluation facilitated by atomistic models.

Electron tomography is an advanced transmission electron microscopy (TEM) technique that captures three-dimensional

* Address correspondence to peter.ciesielski@nrel.gov, bryon.donohoe@nrel.gov.

Received for review June 21, 2013 and accepted August 29, 2013.

Published online August 29, 2013
10.1021/nn4031542

© 2013 American Chemical Society

(3D) structure and is used to bridge the gap between atomic resolution normally provided by X-ray crystallography and whole-system imaging provided by light microscopy, making it a critical tool for materials science^{14,15} and structural biology.^{16,17} Electron tomography can probe the structure of plant cell walls with nanometer resolution, wherein lay critical gaps in our understanding of biomass architecture.¹⁸ At this scale the main structural components of the cell wall, cellulose microfibrils, hemicelluloses, pectins, and lignins, interact to form a complex, composite polymer matrix. Recent studies have demonstrated the applicability of electron tomography to investigate the 3D structure of cell walls in wood and corn stover,^{19–21} however, the analysis of the tomographic data sets in these studies was done by manual, user driven segmentation and surface generation and resulted in predominantly qualitative conclusions. In contrast, the approach presented here employs algorithmic optimization to extract quantitative mathematical descriptions for the longitudinal axes of cellulose microfibrils in the form of parametric space curves. This analysis directly addresses the paucity in the literature surrounding the longitudinal axis of plant microfibrils, and enables measurement of nanoscale curvature of microfibrils for the first time. From these measurements and the crystal structure of cellulose I β ,²² we construct atomistic models of cellulose microfibrils with realistic nanoscale geometries and we show by energy minimization of the atomic coordinates that longitudinal curvature impacts the crystal orientation. While the computational methodology introduced here is general and will enable future studies of microfibril structure from various species and thermochemical treatments, as well as filamentous nanostructures from other biological and nonbiological systems, we choose to demonstrate these techniques on industrially relevant feedstocks and pretreatments so that the results presented herein are of inherent utility to current bioprocessing technologies.

RESULTS AND DISCUSSION

Transmission Electron Microscopy Reveals Biomass Nanostructure after Thermochemical Pretreatment. Changes in biomass structure resulting from thermochemical pretreatment may be observed in general by TEM (Figure 1), which makes this technique/substrate combination an effective platform for the observation nanostructural geometry. A micrograph showing cell walls of native corn stover is presented in Figure 1a. In this state, microscale features such as the compound middle lamella and secondary cell wall may be delineated, but the dense cell wall matrix appears largely homogeneous and its nanostructure is difficult to discern. Figure 1b shows a TEM micrograph of similar cell walls following thermochemical pretreatment by dilute sulfuric acid with an iron sulfate co-catalyst in a steam explosion reactor (DA/Fe).^{23,24} Corn stover treated by

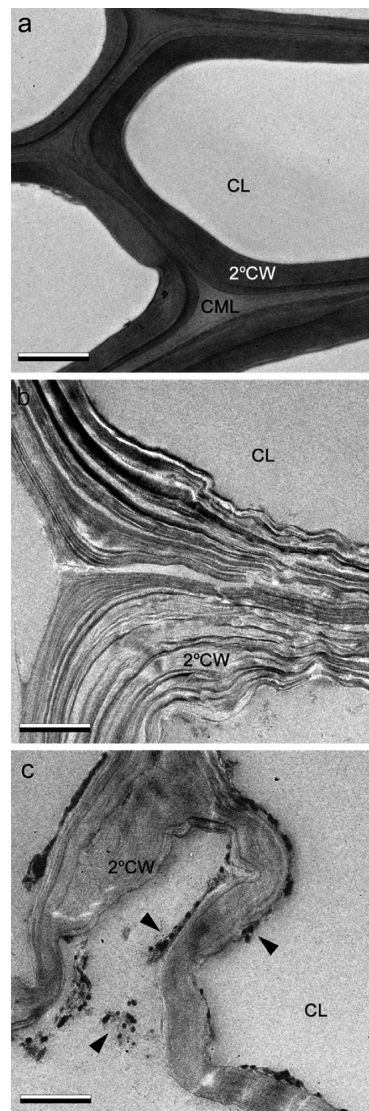


Figure 1. Transmission electron microscopy of native and pretreated corn stover cell walls. (a) Native corn stover cell walls appear dense with little intra-wall void space. Thermochemical treatments by dilute sulfuric acid with an iron co-catalyst (b) and ammonia fiber expansion (c) loosen the cell wall matrix, relocate lignin, and cause delamination of the cell walls. Arrowheads indicate surface deposited lignin–carbohydrate complexes; CL, cell lumen; CML, compound middle lamella; 2°CW, secondary cell wall; scale bars 2 μ m.

ammonia fiber expansion (AFEX)^{25,26} is shown in Figure 1c. Both of these treatments loosen the cell wall matrix, relocate lignin, and allow expansion, delamination, and nanofibrillation of the walls in some regions. These treatments not only enhance the accessibility of the cellulose to enzymes,^{26–29} but also enable the observation of the network of cellulose microfibrils that compose the remaining nanoscale scaffolding of the cell wall. While the alkaline AFEX treatment increases the accessibility of cellulose microfibrils and relocates cell wall matrix polymers, it does not hydrolyze hemicellulose to soluble sugars to the extent DA/Fe treatment does, which removes the vast majority of hemicelluloses, pectins, and proteins into a liquid

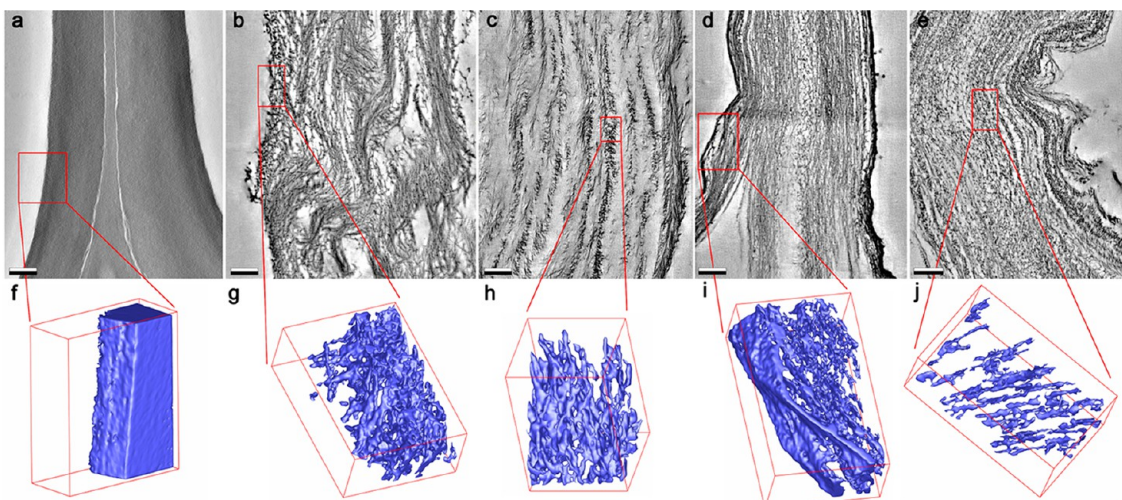


Figure 2. TEM tomography of native and thermochemically treated corn stover cell walls. Slices of tomographic volumes from native corn stover cell walls (a) and those treated by DA/Fe (b and c) and AFEX (d and e); scale bars 200 nm. Surface renditions of subvolumes from the luminal surfaces (f, g, i) show variations in surface texture observed between sample types. Surface renditions from the secondary cell wall interior of DA/Fe-treated (h) and AFEX-treated (j) samples reveal the filamentous structures of cellulose microfibrils and globular residual matrix material.

stream during pretreatment.²⁴ Similar to previous investigations of AFEX-treated material,²¹ assemblies of relocated lignin and hemicelluloses, termed lignin–carbohydrate complexes,³⁰ (LCCs) were observed in abundance as agglomerates of globular material in a disordered, fibrous network located in close proximity to cell wall surfaces. Additional, higher-magnification TEM images of LCCs from AFEX-treated material included in Supporting Information Figure S7 further visualize how this treatment relocates cell wall matrix material but does not remove it from the system.

TEM Tomography Provides 3D Reconstructions of Nanoscale Morphology. Transmission electron tomography was employed to quantitatively investigate the three-dimensional nanostructure of the pretreated cell walls and the cellulose microfibrils. Figure 2a–e compares slices from tomographic reconstructions of cell walls of native corn stover (Figure 2a) and those treated by DA/Fe (Figure 2b,c), and AFEX (Figure 2d,e). Videos visualizing these volumes are presented in Supporting Information V1–V5. Surface renditions of subvolumes from these tomograms shown in Figure 2f–j provide a three-dimensional illustration of the architecture of the pretreated cell walls in contrast to the dense, largely nonporous nature of the native material. The luminal surfaces shown in Figure 2f,g,i represent the cell wall surface that would be directly exposed to enzymes and other homogeneous catalysts. The untreated cell wall surface is relatively smooth and nonporous, while the surface of the pretreated cell walls generally display enhanced porosity and provide channels for catalyst transport to the cell wall interior; however, the film of relocated lignin that was observed on many surfaces of the AFEX-treated walls is evidenced by the thin, dense layer observed in Figure 2i. Both pretreated samples exhibit dramatic increases in void space in the cell wall

interior as shown by the surface renditions shown in Figure 2h,j. To quantify the extent of this phenomenon, the intra-wall void fraction was calculated directly for each tomogram as described in detail in Supporting Information. These results are presented in Table 1. Both pretreatment techniques impart order-of-magnitude increases in intra-wall void space, which dramatically enhances the catalyst-accessible surface area of the biomass and contributes to improved conversion observed for these pretreatments. In a previous microscopy-based investigation of the structure AFEX-treated corn stover, tomographic reconstructions were used to calculate surface-area-to-volume ratios.²¹ While the differences in the dimensionality of these derived measurements preclude their direct quantitative comparison, similar trends were observed wherein effective AFEX pretreatments result in substantial surface-area-to-volume ratios within the cell wall.

Parametric Space Curves Were Fit to the Longitudinal Geometry of Cellulose Microfibrils in the Tomographic Data. While filamentous structures are clearly observable in the tomographic data, their bundled geometries combined with the globular nature of the residual matrix material posed significant challenges to modeling these structures by conventional, manually implemented segmentation methods such as traditional IMOD modeling.³¹ Furthermore, each individual microfibril exhibits a unique, longitudinal geometry at the nanoscale, which precludes the application of tomographic image averaging techniques wherein many subvolumes containing assumed identical structures are averaged together to enhance resolution of a single reconstruction.³² To address these challenges, we developed a model wherein the geometries of the fibril axes are approximated by parametric space curves fit to the tomographic density. We employed the following set of parametric equations to

TABLE 1. Quantitative Analysis of Cell Intra-Wall Void Space and Microfibril Geometry

cell wall treatment	intra-wall void space (%) ^a	number of fitted fibrils	average nearest-neighbor fibril spacing (nm) ^a	average radius of curvature (nm) ^a
None	3.3 ± 7.2			
DA/Fe	62 ± 22	25	22 ± 10	399 ± 281
AFEX	52 ± 15	23	30 ± 5	269 ± 115

^a Reported values represent the mean and standard deviation of the measurements, respectively.

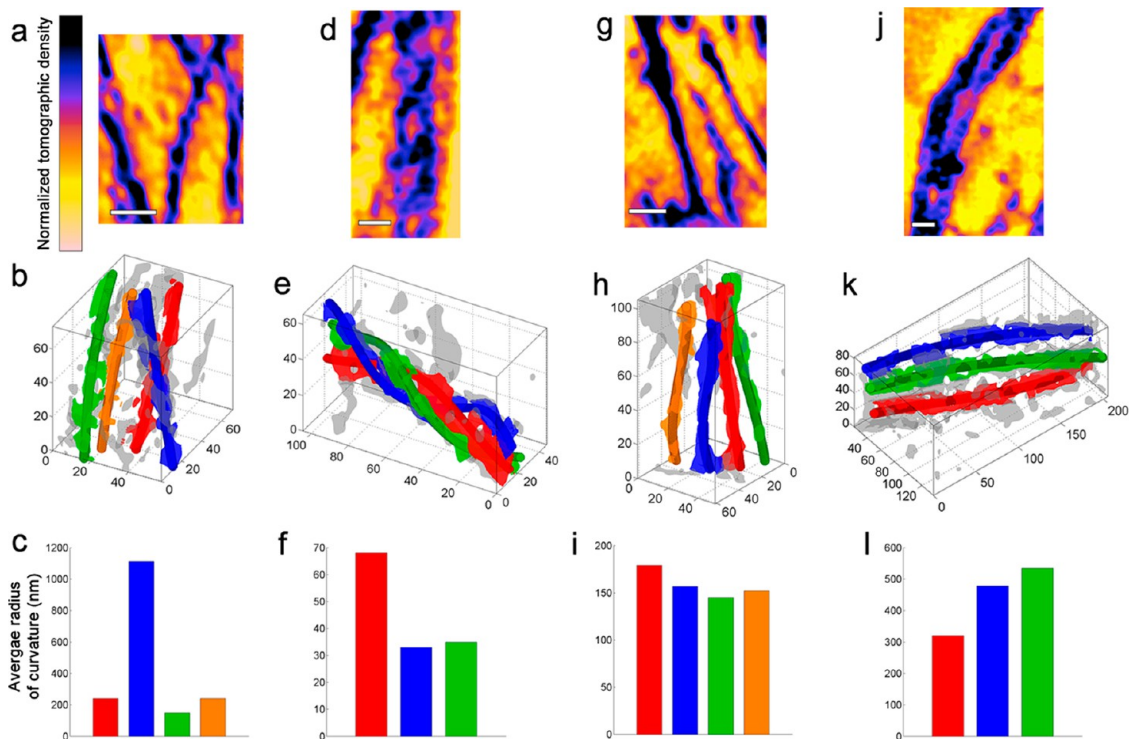


Figure 3. Parametric space curves fit to tomographic subvolumes. Parametric space curves were fit to tomographic densities to extract approximate mathematical descriptions for the geometry of the cellulose microfibrils present within subvolumes of the biomass specimen. (a, d, g, j) Slices through the tomographic subvolumes were oriented to show filamentous structures. Images were normalized to the density range of the slice and false colored to highlight gradients in tomographic density; all scale bars are 20 nm. Videos demonstrating the fitting of space curves to these volumes are included in Supporting Information V6 and V7. (b, e, h, k) The resultant fitted space curves, with surface representations of the tomographic density, are shown below each corresponding tomographic slice; plot units are nm. (c, f, i, l) The average radii of curvature from each fitted space curve are plotted with colors corresponding to the curves shown in the fitted subvolumes above. Slices, fitted subvolumes, and radii of curvature presented in panels a–f are from DA/Fe-treated material, and those presented in panels g–l are from AFEX-treated material.

describe these space curves in the rectangular coordinate system of the tomographic data:

$$\mathbf{h}(t) \equiv \begin{cases} x = c_1 \sin(\omega t + \phi) + P_x(t) \\ y = c_2 \sin(\omega t + \phi) + P_y(t) \\ z = t \end{cases} \quad (1)$$

where $\mathbf{h}(t)$ is an xyz triple that defines the point of a space curve \mathbf{h} at the parameter value of t . The trigonometric operators allow the space curve to adopt a helical geometry with x and y amplitudes (c_1, c_2), phase shift (ω), and angular frequency (ϕ). The terms $P_x(t)$ and $P_y(t)$ are polynomials that afford the curve the flexibility to bend through space as required by the geometry of microfibrils present in the tomographic volumes.

Subsequently, a two-phase fitting algorithm was designed to fit the geometric model described by eq 1

to the tomographic data. In brief, the first phase of the algorithm attempts to place space curves through the most dense regions of the tomogram, and the second phase refines their positions and prevents multiple curves from converging upon the same location. This fitting procedure is described in detail in Supporting Information, and we strongly encourage the reader to view Supporting Videos V6 and V7 which visualize examples of the convergence of this algorithm within several tomographic subvolumes. While this method does not explicitly differentiate tomographic density of cellulose from that of residual hemicelluloses or lignin, it does estimate paths of cellulose microfibrils since other biopolymers in the cell wall cannot themselves exhibit long-range, directional order without the supporting architecture of the cellulose microfibrils.

Subvolumes containing fibrous structures continuously observable through one spatial dimension were selected for analysis. The algorithm was used to fit space curves to 3 subvolumes from each of the tomograms of pretreated corn stover presented in Figure 2b–e. A total of 12 subvolumes were fit (6 from each pretreatment type) to extract geometry for 24 microfibrils from DA/Fe-treated material and 25 microfibrils from AFEX treated material. Figure 3 presents 4 fitted subvolumes and the remaining 8 are included in Supporting Information Figures S3 and S4. To avoid oversampling of specific regions of the cell wall and to facilitate equitable comparison of geometric parameters between pretreatment types, care was taken to select subvolumes from regions in each tomogram that spanned the cell wall in terms of general proximity to the cell lumen. Qualitatively, the observed nanoscale geometries of the microfibrils may be described as always curved, often bundled, but never straight over the length scales investigated here, which is consistent with previous observations of the 3D configuration of microfibrils in plant cell walls.¹⁹ In some regions, such as that shown in Figure 3d,e, helical bundles of microfibrils were observed. Similar structures have been reported previously for cellulose microfibrils in both natural³³ and synthetic³⁴ systems.

The curvature and radius of curvature, denoted as κ and r_κ , respectively, were calculated for each fitted space curve as

$$\kappa(t) = \left\| \frac{d\mathbf{T}}{ds} \right\| = \frac{1}{r_\kappa(t)} \quad (2)$$

where \mathbf{T} is the unit tangent vector and s is arc length. Additional mathematical detail of this calculation is included in Supporting Information. These values were calculated as a function of the parametric variable down the length of each curve, and the average radius of curvature for each fitted curve is plotted in bottom row of Figure 3. These results demonstrate the capability of this methodology to extract the unique, nanoscale geometry of individual microfibrils. The nearest-neighbor distance was also calculated for each fitted curve (as detailed in the Supporting Information). The combined averages of the radii of curvature and nearest-neighbor distances from each pretreatment type are presented in Table 1. While the average radius of curvature is smaller and the average nearest neighbor spacing is larger for AFEX pretreatment, these measures are not statistically different for the sample size investigated in this study, which is perhaps surprising since these two pretreatment techniques employ different chemical conditions. Furthermore, all of the radii of curvatures measured from the microfibrils in these data are much smaller than the radii of cell lumen in maize (which are on the order of tens of micrometers), which demonstrates that the longitudinal geometry of the microfibrils in these materials is not solely dictated by the higher order geometry of the entire cell wall.

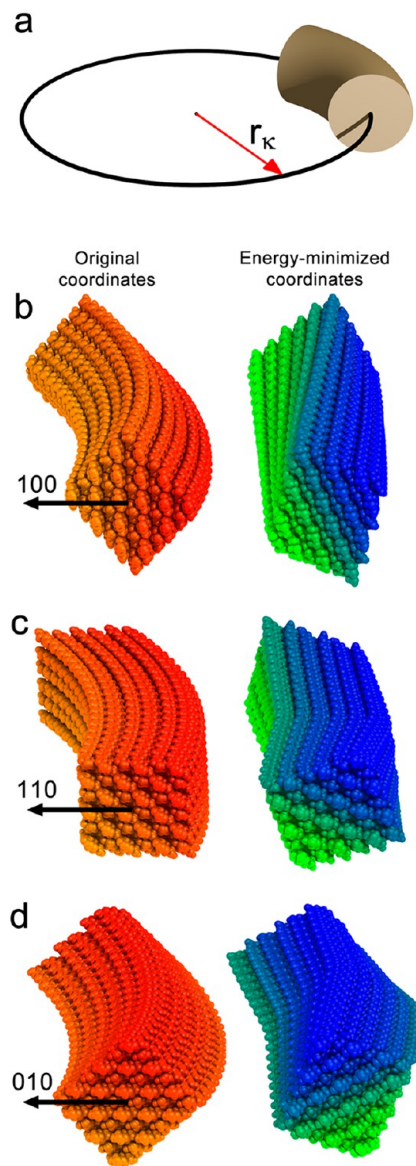


Figure 4. Kink formation in atomistic models of cellulose microfibrils bent about 110 and 010 crystal planes. Atomistic models were constructed to exhibit constant curvature as shown schematically (a). The coordinates were oriented such that the bending occurred about the 100 (b), 110 (c), and 010 (d) crystal planes. The original ideal structures, shown on the left of each panel in warm colors, are bent by a constant radius of curvature of 50 nm. Energy minimization (shown on the right of each panel in cool colors) resulted in the formation of kinks in the models bent by magnitudes above a critical threshold about the 110 and 010 planes as shown in Figure S6. Kink formation was not observed in structures that were bent about the 100 plane.

The Nanoscale Curvature of a Cellulose Microfibril Impacts Its Molecular Orientation. To investigate the impact of the measured nanoscale curvature on the crystal structure of plant cellulose, we constructed models of 36-chain microfibrils³⁵ based on the crystal structure of the I β polymorph²² bent about the 100, 110, and 010 planes of the crystal by a range of constant curvatures. While cell walls have been shown to contain a mixture of both I α and I β polymorphs, the majority of the cellulose exists

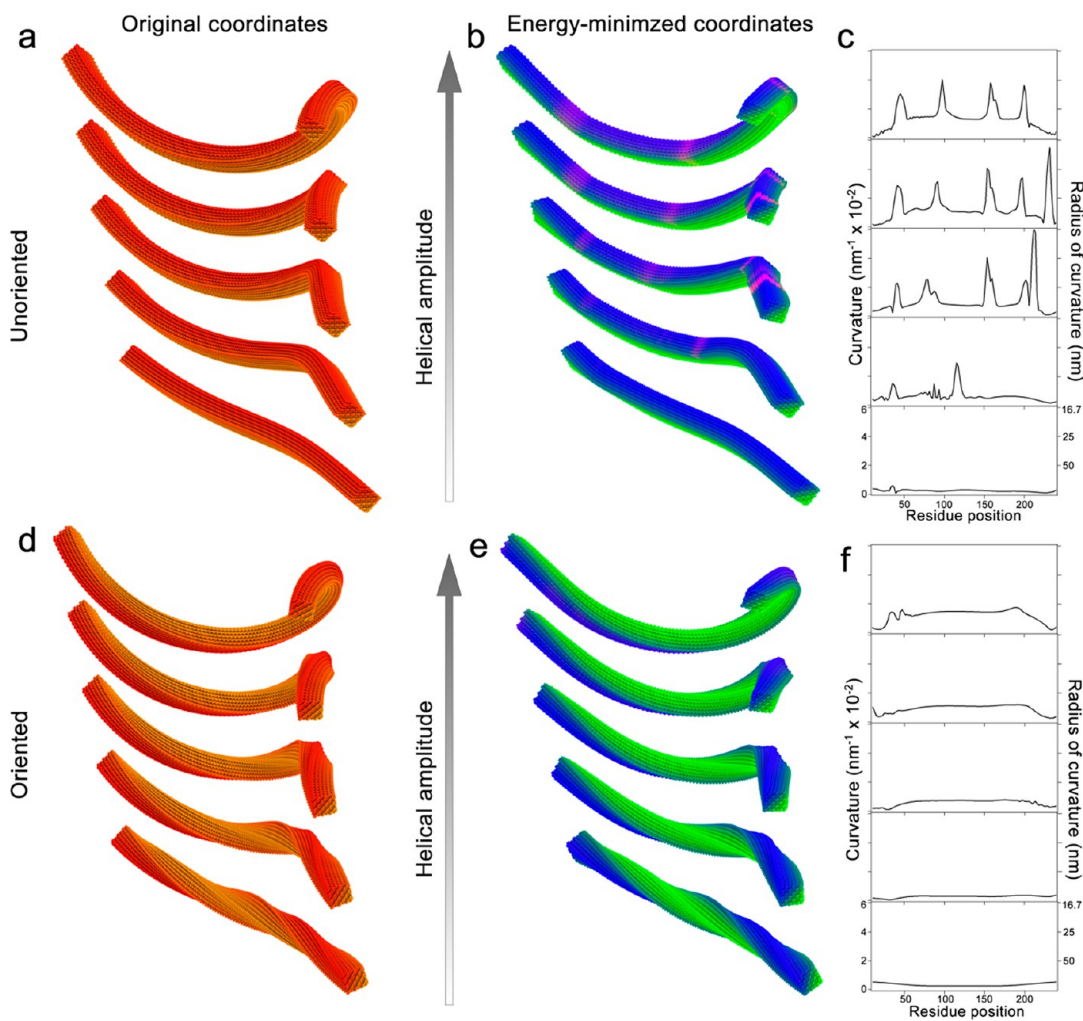


Figure 5. Orienting the crystal structure of the atomic models to bend about the 100 plane prevents kink formation. Large (~ 130 nm) atomistic models were constructed with helical longitudinal geometries to produce structures with constant curvatures. (a) Models were constructed with curvatures that spanned a range of $\sim 0.002 \text{ nm}^{-1}$ ($r_\kappa \approx 500$ nm) to $\sim 0.015 \text{ nm}^{-1}$ ($r_\kappa \approx 67$ nm). The models were relaxed by energy minimization of the atomic coordinates, which caused kink defects to form in the crystal structures of the nontwisted models (b), which are observed as spikes in the curvatures plotted (c). Constructing atomistic models that twist to orient the 100 plane perpendicular to the normal vector of the longitudinal axis (d) prevents the formation of kinks after energy minimization as shown by the structures (e) and corresponding curvatures plotted (f). The relaxed structures shown in panels b and e are highlighted with magenta in proportion to the curvature at each residue position.

in the β polymorph, which was selected to represent the atomic structure of the models presented in this study. Following their construction, the atomic coordinates were relaxed by energy-minimization with CHARMM.³⁶ Selected original and energy-minimized structures are presented in Figure 4 (the entire set of original and energy-minimized structures is included in Supporting Information Figure S6). Relaxation of structures that were bent about the 110 and 010 planes by radii of curvature less than 72 and 85 nm, respectively, caused the formation of kinks, or abrupt spikes in curvature that indicate defects in the crystal structure. Interestingly, relaxation of structures bent about the 100 crystal planes did not result in kink formation for any of the radii of curvature investigated among these structures, and the crystal structure developed a right-handed twist as observed in previous studies.^{35,37,38} Microfibril kinks were evident, however rare,

in the tomographic data (examples of kinked microfibrils from each pretreatment type are shown in Supporting Information Figure S8). In these pretreated materials, kinks such as those shown in Figure S8 are likely caused by the mechanical action of milling or explosive decompression, and will produce large disruptions in the cellulose structure. Recent studies have shown that kinked geometry at the cell wall scale induced by mechanical processing promotes catalytic hydrolysis,³⁹ which identifies these as important structural targets for efficient conversion of cellulose and warrants additional investigation. Furthermore, kink defects in the cellulose crystals such as those predicted by this method may also contribute to the level-off degree of polymerization (LODP) observed as a result of acid hydrolysis;⁴⁰ however, additional experiments are required to adequately elucidate the relationship between these phenomena.

The effect of kink formation on larger microfibrils was investigated by constructing models \sim 130 nm in length (250 glucose residues per chain). Employing helical longitudinal geometries allowed the construction of models with constant curvature while avoiding self-intersection. Models were constructed with a range of helical amplitudes at a frequency equal to that observed in the subvolume presented in Figure 3d,e, such that each structure had essentially constant curvature. As one traces a path down the length of a helical space curve, the unit normal vector rotates about the unit tangent vector at the frequency of the trigonometric operators used to generate the curve. Therefore, a non-twisted microfibril model translated by a helical space curve experiences bending about each of its crystal planes as the unit normal vector rotates about the longitudinal axis of the crystal. Models constructed in this manner are presented before and after relaxation by energy minimization in Figure 5a,b, and the curvature of the relaxed structure is plotted against residue position in Figure 5c. These structures form kinks similar to those displayed by the shorter models. An additional set of models was constructed by the same helical geometries, but the atomic structures of these models were oriented such that 100 crystal plane remained perpendicular to the unit normal vector, which imparts a twist to the crystal. These oriented models are presented before and after relaxation in Figure 5d,e, and the corresponding curvatures of the relaxed structures are plotted in Figure 5f. Videos that visualize the construction of oriented and nonoriented structures are included in Supporting Information V8 and V9 to further demonstrate the difference between these sets of models. As shown in Figure 5e, relaxation of the oriented, or effectively twisted, structures produced significantly fewer regions of extreme curvature than the nonoriented models, which allowed the relaxed microfibrils to retain relatively constant curvature. These results suggest an important structure–property relationship for plant cellulose microfibrils, namely, that twisting about the longitudinal axis of the microfibril may provide a means to accommodate

moderate nanoscale curvature while minimizing defect formation within the cellulose crystal. Such continual reorientations of the crystal structure along the longitudinal axis could indeed give rise to the loss of crystallographic coherence in this dimension as suggested previously.¹⁸ These large atomistic models that exhibit nanoscale geometry representative of experimental data have utility for developing accurate coarse-grained models that facilitate large scale simulations,^{41–44} which heretofore have not incorporated nanoscale curvature.

CONCLUSIONS

In summary, we have extracted mathematical representations for the nanoscale geometry of cellulose microfibrils in pretreated biomass from tomographic data sets. The resulting parametric equations were used to calculate the curvature of plant cellulose microfibrils for the first time. These results were used in conjunction with the crystal structure of cellulose I β to propose and evaluate atomistic models for microfibrils that incorporated the geometric parameters observed in the tomographic data. We found that orienting microfibril models to bend about the 100 crystal plane reduced the formation of kink defects after energy minimization. The connection between directly observed, nanoscale geometry and proposed atomistic models established by this methodology will be further informed and improved by the incorporation of new findings and extension to new applications. Much work remains in order to achieve more complete and extensively validated atomistic models of biomass nanostructure, especially in the native state. Additional progress in 3D nanoscale imaging, sample preparation, and quantitative image analysis are needed to conclusively segment and model the structures of hemicelluloses and lignin in the cell wall, which will inform and synergize with future atomistic and coarse-grained simulation efforts. Nevertheless, the detailed models of plant cellulose constructed from the data and methods in this work constitute a foundational step toward experimentally derived, atomic models of biomass nanostructure.

METHODS

Biomass Pretreatment. DA/Fe pretreatment was carried out using methods previously reported.^{23,24} Briefly, corn stover (Pioneer variety 33A14) from the Kramer farm in Wray, Colorado was tub ground, then milled through a Mitts & Merrill rotary knife mill (model 10 \times 12) to pass a 1/4-in. screen. Acid impregnation was carried out using 120 L of \sim 45 °C 0.5 wt % H₂SO₄ in a 200-L recirculation tank. For dilute-acid/Fe³⁺ ion co-catalyst impregnation, the acid was equilibrated for 4 h in the recirculating bath. A Hastelloy C-276 wire 20 mesh basket was loaded with 14.5 kg of 1/4-in. milled corn stover feedstock (\sim 94% solids) and lowered into the bath of warm dilute acid/Fe³⁺ ion co-catalyst for 2 h. The biomass was drained of excess acid to approximately 20% solids and loaded into a hydraulic dewatering press where the acid impregnated feedstock was pressed to \sim 45% solids. A 4-L Hastelloy steam explosion reactor was prewarmed to pretreatment

temperature and was loaded with 500.0 g of dilute-acid/Fe³⁺ ion co-catalyst impregnated and pressed feedstock (\sim 45% solids) and quickly heated (\sim 5–10 s) via direct steam injection to 150 °C. At 15 min, the pretreated feedstock was rapidly depressurized to atmospheric pressure and blown into a flash tank.

AFEX pretreatment was carried out as described previously.²¹ Briefly, pretreatment on NREL corn stover was conducted in a 2 L Parr reactor (316 SS, PARR Instrument Co., Moline, IL). The reactor was clamped shut and 1:1 ammonia to biomass loading was injected using a preweighed ammonia delivery vessel. The reactor was heated using a custom aluminum block on a hot plate and maintained at 130 °C for 15 min. At the end of the residence time, the pressure was explosively released. The biomass was removed from the reactor and left overnight to remove the residual ammonia.

Sample Preparation for TEM and Image Acquisition. Pretreated biomass samples were processed using microwave EM

processing. Samples were fixed 2×6 min (2 min on, 2 min off, 2 min on) in 2.5% gluteraldehyde buffered in 0.1 M sodium cacodylate buffer (EMS, Hatfield, PA). The samples were dehydrated by treating with increasing concentrations of acetone in Pelco microwave oven for 1 min each dilution (15%, 30%, 60%, 90%, and $3 \times 100\%$ acetone). After dehydration, the samples were infiltrated with Eponate 812 (EMS, Hatfield, PA) by incubating at room temperature (RT) for several hours to overnight in increasing concentrations of resin (15%, 30%, 60%, 90%, $3 \times 100\%$ resin, diluted in acetone). The samples were transferred to capsules and the resin polymerized in and oven at 60°C overnight. Resin embedded samples were sectioned to ~ 50 or 250 nm with a Diatome diamond knife on a Leica EM UTC ultramicrotome (Leica, Wetzlar, Germany). Sections were collected on 0.5% Formvar coated slot grids (SPI Supplies, West Chester, PA). Grids were poststained for 2 min with 1% aqueous KMnO_4 to selectively stain for lignins. Images were taken with a 4 mega-pixel Gatan UltraScan 1000 camera (Gatan, Pleasanton, CA) on a FEI Tecnai G2 20 Twin 200 kV LaB6 TEM (FEI, Hillsboro, OR) using SerialEM.⁴⁵

Tomogram Assembly, Visualization, and Analysis. Tomograms were obtained by first capturing dual-axis $\pm 60^\circ$ tilt series of 2×2 montage frames of the regions of interest at a pixel size of ~ 0.5 nm. Tomograms were constructed from the tilt series using the R-weighted back projection algorithm within the IMOD software package.³¹ Single-axis tomograms were then combined to yield dual-axis tomograms using a warping algorithm.^{45,46} Tomographic volumes were visualized with the IMOD software package. Tomographic subvolumes were imported and displayed in Matlab using functions adapted from the PEET software package.³² The fitting algorithm, parametric equations, cost function, and additional data analysis functions consist of original Matlab code written for this work. Minimization of the cost function was performed using the Matlab simplex function *fminsearch*.

Atomistic Model Construction, Energy Minimization, and Visualization. Atomistic models for cellulose microfibrils were constructed based on the coordinates of the I β polymorph.²² Model crystallite segments were oriented and translated along the ideal model or fitted space curves in Matlab, as described in detail in Supporting Information. Each structure was energy minimized in CHARMM³⁶ using the C35 carbohydrate force field^{47,48} under vacuum, with a spherical nonbond cutoff of 25 Å. For the models in Figures 4 and S6, each structure was energy minimized to convergence by the adopted basis Newton–Raphson method. For the models in Figures 5, each structure was relaxed by the adopted basis Newton–Raphson method for 100 000 steps. Interlayer and surface hydrogen bonds were prevented from forming by using flat-bottom dihedral restraining potentials on all hydroxymethyl and hydroxyl conformations. These potentials applied no restraining forces within deviations of 5 or 30° , respectively, from the initial I β coordinates, and applied a restraining force constant of 40 kcal/mol outside these allowed dihedral rotation limits. Atomic models were visualized using the PYMOL Molecular Graphics System, Version 1.5, Schrödinger, LLC.

Conflict of Interest: The authors declare no competing financial interest.

Acknowledgment. This work was supported by the Center for Direct Catalytic Conversion of Biomass to Biofuels (C3Bio), an Energy Frontier Research Center funded by the U.S. Department of Energy, Office of Science, Office of Basic Energy Sciences under Award Number DE-SC0000997. We would like to thank Xiaowen Chen for assistance preparing the DA/FE pretreated samples and Shishir Chundawat and Leonardo da Costa Sousa from MSU's Biomass Conversion Research Laboratory for providing the AFEX pretreated materials.

Supporting Information Available: Nomenclature and definitions; videos visualizing the tomographic data sets; additional mathematical detail for all of the following: calculation of intra-wall void fraction, nearest-neighbor spacing, curvature/radius of curvature, development and implementation of the fitting algorithm, and construction of atomistic models; videos visualizing the convergence of the fitting algorithm; summary of all fitted subvolumes; videos visualizing the construction of atomistic models; summary of atomic models; TEM images of LCC

complexes; tomographic slices showing kinks found in the tomographic data. This material is available free of charge via the Internet at <http://pubs.acs.org>.

REFERENCES AND NOTES

- Sluiter, J. B.; Ruiz, R. O.; Scarlata, C. J.; Sluiter, A. D.; Templeton, D. W. Compositional Analysis of Lignocellulosic Feedstocks. 1. Review and Description of Methods. *J Agric. Food. Chem.* **2010**, *58*, 9043–9053.
- Avci, U.; Pattathil, S.; Hahn, M. G. Immunological Approaches to Plant Cell Wall and Biomass Characterization: Immunolocalization of Glycan Epitopes. In *Biomass Conversion: Methods and Protocols*; Himmel, M. E., Ed.; Methods in Molecular Biology: Humana Press, Springer: New York, **2012**; Vol. 908, pp 73–82.
- McCann, M. C.; Carpita, N. C. Designing the Deconstruction of Plant Cell Walls. *Curr. Opin. Plant Biol.* **2008**, *11*, 314–320.
- Himmel, M. E.; Ding, S. Y.; Johnson, D. K.; Adney, W. S.; Nimlos, M. R.; Brady, J. W.; Foust, T. D. Biomass Recalcitrance: Engineering Plants and Enzymes for Biofuels Production. *Science* **2007**, *315*, 804–807.
- Graham-Rowe, D. Agriculture: Beyond Food versus Fuel. *Nature* **2011**, *474*, S6–S8.
- Mosier, N.; Wyman, C.; Dale, B.; Elander, R.; Lee, Y. Y.; Holtzapple, M.; Ladisch, M. Features of Promising Technologies for Pretreatment of Lignocellulosic Biomass. *Bioresour. Technol.* **2005**, *96*, 673–686.
- Chundawat, S. P. S.; Bellesia, G.; Uppugundla, N.; Sousa, L. D.; Gao, D. H.; Cheh, A. M.; Agarwal, U. P.; Bianchetti, C. M.; Phillips, G. N.; Langan, P.; et al. Restructuring the Crystalline Cellulose Hydrogen Bond Network Enhances Its Depolymerization Rate. *J. Am. Chem. Soc.* **2011**, *133*, 11163–11174.
- Beckham, G. T.; Matthews, J. F.; Peters, B.; Bomble, Y. J.; Himmel, M. E.; Crowley, M. F. Molecular-Level Origins of Biomass Recalcitrance: Decrystallization Free Energies for Four Common Cellulose Polymorphs. *J. Phys. Chem. B* **2011**, *115*, 4118–4127.
- Warden, A.; Little, B.; Haritos, V. A Cellular Automaton Model of Crystalline Cellulose Hydrolysis by Cellulases. *Biotechnol. Biofuels* **2011**, *4*, 39.
- Zhou, W.; Schutte, H. B.; Hao, Z. Q.; Xu, Y. Cellulose Hydrolysis in Evolving Substrate Morphologies I: A General Modeling Formalism. *Biotechnol. Bioeng.* **2009**, *104*, 261–274.
- Bansal, P.; Hall, M.; Realff, M. J.; Lee, J. H.; Bommarius, A. S. Modeling Cellulase Kinetics on Lignocellulosic Substrates. *Biotechnol. Adv.* **2009**, *27*, 833–848.
- Somerville, C.; Bauer, S.; Brininstool, G.; Facette, M.; Hamann, T.; Milne, J.; Osborne, E.; Paredez, A.; Persson, S.; Raab, T.; et al. Toward a Systems Approach to Understanding Plant-Cell Walls. *Science* **2004**, *306*, 2206–2211.
- Ding, S. Y.; Liu, Y. S.; Zeng, Y. N.; Himmel, M. E.; Baker, J. O.; Bayer, E. A. How Does Plant Cell Wall Nanoscale Architecture Correlate with Enzymatic Digestibility? *Science* **2012**, *338*, 1055–1060.
- Batenburg, K. J.; Bals, S.; Sijbers, J.; Kubel, C.; Midgley, P. A.; Hernandez, J. C.; Kaiser, U.; Encina, E. R.; Coronado, E. A.; Van Tendeloo, G. 3d Imaging of Nanomaterials by Discrete Tomography. *Ultramicroscopy* **2009**, *109*, 730–740.
- Ersen, O.; Hirlimann, C.; Drillon, M.; Werckmann, J.; Tihay, F.; Pham-Huu, C.; Crucifix, C.; Schultz, P. 3d-Tem Characterization of Nanometric Objects. *Solid State Sci.* **2007**, *9*, 1088–1098.
- Leis, A.; Rockel, B.; Andrees, L.; Baumeister, W. Visualizing Cells at the Nanoscale. *Trends Biochem. Sci.* **2009**, *34*, 60–70.
- McIntosh, R.; Nicastro, D.; Mastronarde, D. New Views of Cells in 3d: An Introduction to Electron Tomography. *Trends Cell Biol.* **2005**, *15*, 43–51.
- Fernandes, A. N.; Thomas, L. H.; Altaner, C. M.; Callow, P.; Forsyth, V. T.; Apperley, D. C.; Kennedy, C. J.; Jarvis, M. C. Nanostructure of Cellulose Microfibrils in Spruce Wood. *Proc. Natl. Acad. Sci. U.S.A.* **2011**, *108*, E1195–E1203.

19. Xu, P.; Donaldson, L. A.; Gergely, Z. R.; Staehelin, L. A. Dual-Axis Electron Tomography: A New Approach for Investigating the Spatial Organization of Wood Cellulose Microfibrils. *Wood Sci. Technol.* **2007**, *41*, 101–116.
20. Donohoe, B. S.; Decker, S. R.; Tucker, M. P.; Himmel, M. E.; Vinzant, T. B. Visualizing Lignin Coalescence and Migration through Maize Cell Walls Following Thermochemical Pretreatment. *Biotechnol. Bioeng.* **2008**, *101*, 913–925.
21. Chundawat, S. P. S.; Donohoe, B. S.; Sousa, L. D.; Elder, T.; Agarwal, U. P.; Lu, F. C.; Ralph, J.; Himmel, M. E.; Balan, V.; Dale, B. E. Multi-Scale Visualization and Characterization of Lignocellulosic Plant Cell Wall Deconstruction during Thermochemical Pretreatment. *Energy Environ. Sci.* **2011**, *4*, 973–984.
22. Nishiyama, Y.; Langan, P.; Chanzy, H. Crystal Structure and Hydrogen-Bonding System in Cellulose I Beta from Synchrotron X-Ray and Neutron Fiber Diffraction. *J. Am. Chem. Soc.* **2002**, *124*, 9074–9082.
23. Nguyen, Q. A.; Tucker, M. P. Dilute Acid/Metal Salt Hydrolysis of Lignocellulosics. US Patent 6423145, 2002.
24. Wei, H.; Donohoe, B.; Vinzant, T.; Ciesielski, P.; Wang, W.; Gedvilas, L.; Zeng, Y.; Johnson, D.; Ding, S.-Y.; Himmel, M.; et al. Elucidating the Role of Ferrous Ion Cocatalyst in Enhancing Dilute Acid Pretreatment of Lignocellulosic Biomass. *Biotechnol. Biofuels* **2011**, *4*, 48.
25. Chundawat, S. P. S.; Vismeh, R.; Sharma, L. N.; Humpula, J. F.; da Costa Sousa, L.; Chambliss, C. K.; Jones, A. D.; Balan, V.; Dale, B. E. Multifaceted Characterization of Cell Wall Decomposition Products Formed During Ammonia Fiber Expansion (Afex) and Dilute Acid Based Pretreatments. *Bioresour. Technol.* **2010**, *101*, 8429–8438.
26. Teymour, F.; Laureano-Perez, L.; Alizadeh, H.; Dale, B. E. Optimization of the Ammonia Fiber Explosion (Afex) Treatment Parameters for Enzymatic Hydrolysis of Corn Stover. *Bioresour. Technol.* **2005**, *96*, 2014–2018.
27. Himmel, M. E. Biomass Recalcitrance: Engineering Plants and Enzymes for Biofuels Production. *Science* **2007**, *316*, 982–982.
28. Langan, P.; Gnanakaran, S.; Rector, K. D.; Pawley, N.; Fox, D. T.; Cho, D. W.; Hammel, K. E. Exploring New Strategies for Cellulosic Biofuels Production. *Energy Environ. Sci.* **2011**, *4*, 3820–3833.
29. Jeoh, T.; Ishizawa, C. I.; Davis, M. F.; Himmel, M. E.; Adney, W. S.; Johnson, D. K. Cellulase Digestibility of Pretreated Biomass Is Limited by Cellulose Accessibility. *Biotechnol. Bioeng.* **2007**, *98*, 112–122.
30. Morrison, I. M. Structural Investigations on Lignin-Carbohydrate Complexes of Lolium-Perenne. *Biochem. J.* **1974**, *139*, 197–204.
31. Kremer, J. R.; Mastronarde, D. N.; McIntosh, J. R. Computer Visualization of Three-Dimensional Image Data Using Imod. *J. Struct. Biol.* **1996**, *116*, 71–6.
32. Nicastro, D.; Schwartz, C.; Pierson, J.; Gaudette, R.; Porter, M. E.; McIntosh, J. R. The Molecular Architecture of Axonemes Revealed by Cryo-electron Tomography. *Science* **2006**, *313*, 944–948.
33. Ruben, G. C.; Bokelman, G. H. Triple-Stranded, Left-Hand-Twisted Cellulose Microfibril. *Carbohydr. Res.* **1987**, *160*, 434–443.
34. Canejo, J. P.; Borges, J. P.; Godinho, M. H.; Brogueira, P.; Teixeira, P. I. C.; Terentjev, E. M. Helical Twisting of Electrospun Liquid Crystalline Cellulose Micro- and Nanofibers. *Adv. Mater.* **2008**, *20*, 4821–4825.
35. Matthews, J. F.; Beckham, G. T.; Bergenstrahle-Wohlt, M.; Brady, J. W.; Himmel, M. E.; Crowley, M. F. Comparison of Cellulose I Beta Simulations with Three Carbohydrate Force Fields. *J. Chem. Theory Comput.* **2012**, *8*, 735–748.
36. Brooks, B. R.; Brooks, C. L.; Mackerell, A. D.; Nilsson, L.; Petrella, R. J.; Roux, B.; Won, Y.; Archontis, G.; Bartels, C.; Boresch, S.; et al. CHARMM: The Biomolecular Simulation Program. *J. Comput. Chem.* **2009**, *30*, 1545–1614.
37. Matthews, J. F.; Skopec, C. E.; Mason, P. E.; Zuccato, P.; Torget, R. W.; Sugiyama, J.; Himmel, M. E.; Brady, J. W. Computer Simulation Studies of Microcrystalline Cellulose I Beta. *Carbohydr. Res.* **2006**, *341*, 138–152.
38. Paavilainen, S.; Rog, T.; Vattulainen, I. Analysis of Twisting of Cellulose Nanofibrils in Atomistic Molecular Dynamics Simulations. *J. Phys. Chem. B* **2011**, *115*, 3747–3755.
39. Hidayat, B. J.; Felby, C.; Johansen, K. S.; Thygesen, L. G. Cellulose Is Not Just Cellulose: A Review of Dislocations as Reactive Sites in the Enzymatic Hydrolysis of Cellulose Microfibrils. *Cellulose* **2012**, *19*, 1481–1493.
40. Battista, O.; Coppick, S.; Howson, J.; Morehead, F.; Sisson, W. A. Level-Off Degree of polymerization. *Industrial & Engineering Chemistry* **1956**, *48*, 333–335.
41. Chang, R.; Gross, A. S.; Chu, J. W. Degree of Polymerization of Glucan Chains Shapes the Structure Fluctuations and Melting Thermodynamics of a Cellulose Microfibril. *J. Phys. Chem. B* **2012**, *116*, 8074–8083.
42. Wohlt, J.; Berglund, L. A. A Coarse-Grained Model for Molecular Dynamics Simulations of Native Cellulose. *J. Chem. Theory Comput.* **2011**, *7*, 753–760.
43. Glass, D. C.; Moritsugu, K.; Cheng, X. L.; Smith, J. C. Reach Coarse-Grained Simulation of a Cellulose Fiber. *Biomacromolecules* **2012**, *13*, 2634–2644.
44. Bu, L.; Beckham, G. T.; Crowley, M. F.; Chang, C. H.; Matthews, J. F.; Bomble, Y. J.; Adney, W. S.; Himmel, M. E.; Nimlos, M. R. The Energy Landscape for the Interaction of the Family 1 Carbohydrate-Binding Module and the Cellulose Surface Is Altered by Hydrolyzed Glycosidic Bonds. *J. Phys. Chem. B* **2009**, *113*, 10994–11002.
45. Mastronarde, D. N. Automated Electron Microscope Tomography Using Robust Prediction of Specimen Movements. *J. Struct. Biol.* **2005**, *152*, 36–51.
46. Mastronarde, D. N. Dual-Axis Tomography: An Approach with Alignment Methods That Preserve Resolution. *J. Struct. Biol.* **1997**, *120*, 343–352.
47. Guvench, O.; Greene, S. N.; Kamath, G.; Brady, J. W.; Venable, R. M.; Pastor, R. W.; Mackerell, A. D. Additive Empirical Force Field for Hexopyranose Monosaccharides. *J. Comput. Chem.* **2008**, *29*, 2543–2564.
48. Guvench, O.; Hatcher, E.; Venable, R. M.; Pastor, R. W.; Mackerell, A. D. CHARMM Additive All-Atom Force Field for Glycosidic Linkages between Hexopyranoses. *J. Chem. Theory Comput.* **2009**, *5*, 2353–2370.